

Anti-angiogenic therapy affects the relationship between tumor vascular structure and function: a correlation study between micro-CT angiography and DCE-MRI

Eugene Kim¹, Jana Kim¹, Gunhild Mari Mælandsmo², Berit Johansen³, Siver Andreas Moestue¹

¹Department of Circulation and Medical Imaging, Norwegian University of Science and Technology, 7491 Trondheim, Norway

²Department of Tumor Biology, Institute for Cancer Research, The Norwegian Radium Hospital, Oslo University Hospital, 0424 Oslo, Norway

³Department of Biology, Norwegian University of Science and Technology, 7491 Trondheim, Norway

Corresponding author: Eugene Kim

MR Cancer Group
Department of Circulation and Medical Imaging
Norwegian University of Science and Technology
P.O. Box 8905
7491 Trondheim
Norway
E-mail: eugene.kim@ntnu.no
Phone: +47 73 59 86 37

Word count: 3714

Running title: Correlation between DCE-MRI and micro-CT angiography in a breast cancer xenograft model

Keywords: anti-angiogenic therapy, DCE-MRI, micro-CT, tumor vasculature

Abstract

Purpose: To compare the effects of two anti-angiogenic drugs, bevacizumab and a cytosolic phospholipase A2-a inhibitor (AVX235), on the relationship between vascular structure and dynamic contrast enhanced (DCE)-MRI measurements in a patient-derived breast cancer xenograft model.

Methods: Mice bearing MAS98.12 tumors were randomized into three groups: bevacizumab-treated ($n=9$), AVX235-treated ($n=9$), and control ($n=8$). DCE-MRI was performed pre-and post-treatment. The median initial area under the concentration-time curve ($IAUC_{60}$) and volume transfer constant (K^{trans}) were computed for each tumor. The tumors were excised for ex vivo micro-CT angiography, from which the vascular surface area (VSA) and fractional blood volume (FBV) were computed. Spearman correlation coefficients (ρ) were computed to evaluate the associations between the DCE-MRI and micro-CT parameters.

Results: With the groups pooled, $IAUC_{60}$ and K^{trans} correlated significantly with VSA ($\rho=0.475$ and 0.527 , $P=0.019$ and 0.008). There were no significant correlations within the control group. There were various significant correlations within the treatment groups but the correlations in the bevacizumab group were of opposite sign, e.g., K^{trans} vs. FBV: AVX235 $\rho=0.800$ ($P=0.014$), bevacizumab $\rho=-0.786$ ($P=0.023$).

Conclusion: DCE-MRI measurements can highly depend on vascular structure. The relationship between vascular structure and function changed markedly after anti-angiogenic treatment.

Keywords: anti-angiogenic therapy, DCE-MRI, micro-CT, tumor vasculature

Introduction

DCE-MRI provides information on vascular function (blood flow, permeability), and DCE-MRI biomarkers are frequently incorporated into clinical trials of anti-angiogenic therapies (1). Currently recommended biomarkers to measure include the initial area under the contrast agent concentration-time curve at 60 seconds post-injection (IAUC_{60}) and the volume transfer constant (K^{trans}) derived from the Tofts model (2-4). Both of these are composite parameters that depend on a combination of blood flow and vessel permeability-surface area product (PS). The dependence of these DCE-MRI parameters on multiple factors can make their physiological interpretations ambiguous. However, they have shown promise as biomarkers of cancer treatment response, suggesting that physiologically specific biomarkers may not be essential for clinical decision making (5).

Still, separate measurements of biological factors can be interesting and helpful, e.g., in studying drug mechanisms of action or in certain clinical cases (6,7). Generalized pharmacokinetic models can provide individual estimates of blood plasma volume fraction (v_p), extravascular-extracellular space volume fraction (v_e), blood flow, and PS (8); but these models have not been widely adopted for DCE-MRI analysis.

Regardless of the method of analysis, DCE-MRI is often discussed in the context of blood flow and permeability (i.e., vascular function) while the surface area component of the PS product (i.e., vascular structure) is largely ignored. A search for “DCE-MRI” on PubMed (August 15, 2016) yielded 1929 results; of those, 246 also include the term “flow”, 342 include “permeability”, and only 40 include “surface area”. This illustrates that relatively few studies have explicitly investigated how vascular morphology influences DCE-MRI measurements or how this relationship is affected by treatment (9-11). (Throughout the manuscript, vascular morphology/structure refer to the “macroscopic” form of the vascular network and not cellular morphology of the endothelium and perivascular components).

In this study, we addressed these questions by comparing *in vivo* DCE-MRI parameters to *ex vivo* micro-CT vascular morphometrics and histology in a patient-derived xenograft model of breast cancer treated with two different anti-angiogenic agents: 1) bevacizumab (Avastin[®], Genentech Inc., South San Francisco, CA, USA), a monoclonal antibody

against vascular endothelial growth factor A, the main driver of tumor angiogenesis (12); and 2) AVX235 (Avexxin AS, Trondheim, Norway), a small molecule inhibitor of group IVA cytosolic phospholipase A₂-a, a pro-inflammatory and pro-angiogenic enzyme that has emerged as a potential therapeutic target in various cancers (13-16).

Methods

Experimental design

MAS98.12 patient-derived basal-like/triple-negative breast cancer xenografts were bilaterally and orthotopically transplanted into the thoracic mammary fat pads of 26 female Hsd:Athymic Nude-Foxn1^{nu} mice. The establishment and maintenance of the tumor model is described in (17). Details of animal housing and handling can be found in (16). All procedures and experiments involving animals were approved by the Norwegian Animal Research Authority and carried out according to the European Convention for the Protection of Vertebrates used for Scientific Purposes.

The mice were randomly assigned to one of three groups when the long axis of the larger tumor reached ~8 mm as measured by calipers. Baseline MRI was performed on all mice (day 0). Afterward, one group ($n = 9$) received bevacizumab (5 mg/kg i.p., 0.5 mg/mL saline) on days 0 and 3; another group ($n = 9$) received daily doses of AVX235 (45 mg/kg i.p., 22.5mg/mL dimethyl sulfoxide) from day 0 to day 6; and a control group ($n = 8$) received daily doses (2 mL/kg) of 100% dimethyl sulfoxide from day 0 to day 6. All mice were scanned again on day 4, after which the bevacizumab-treated mice were sacrificed; AVX235-treated and control mice were scanned again on day 7 before being sacrificed. For the control and AVX235 groups, the DCE-MRI data collected on day 4 was not included in this study.

Previous studies have demonstrated that both drugs inhibit long-term growth of this tumor model (16,18). The short duration of this study was chosen in order to investigate the early vascular effects of the drugs.

MRI

MRI was performed on a 7T scanner (BioSpec 70/20 Avance III, Bruker Biospin, Ettlingen, Germany) using an 86 mm excitation volume coil and a mouse brain quadrature receiver surface coil. The mice were anesthetized with isoflurane (2-2.5% in 67% air/33% O₂, 0.6 L/min); isoflurane levels were adjusted as needed to maintain a respiration rate of ~60 breaths/min. The animals' body temperatures were monitored with a rectal probe and controlled using a small animal monitoring system (Model 1030, SAI, Stony Brook, NY, USA).

A fast low angle shot sequence was used to acquire 3D images for tumor volume measurements: echo time (TE) = 3 ms, repetition time (TR) = 13 ms, flip angle = 30°, 8 averages, matrix = 256×96×48 zero-padded to 256×128×64, field of view = 20×20×10 mm³. High-resolution T2-weighted 2D RARE images were acquired to delineate tumor regions of interest (ROI): TE = 68 ms, TR = 1500 ms, RARE factor = 16, 4 averages, matrix = 256×192 zero-padded to 256×256. A 2D rapid acquisition with relaxation enhancement (RARE) sequence with variable TRs was used to compute baseline T1 maps: effective TE = 13 ms; TR = 225, 500, 1500, 3000, 6000, 12000 ms; RARE factor = 2, matrix = 64×48 zero-padded to 64×64. This was followed by the acquisition of a dynamic series of 200 T1-weighted images using a 2D RARE sequence: effective TE = 7.5 ms, TR = 300 ms, RARE factor = 4, matrix = 64×64, temporal resolution = 4.8 s. An intravenous bolus injection of 0.3 mmol/kg of gadodiamide (Omniscan, GE Healthcare, Oslo, Norway) was administered via the tail vein after the tenth baseline image. All 2D scans were acquired with the same geometry: field of view = 20×20 mm², slice thickness = 0.6 mm, interslice gap = 0.3 mm, 4 coronal slices.

Tumor ROIs, which excluded skin and subcutaneous fat around the tumors, were manually drawn on the 3D images for tumor volume measurements, and on the high-resolution 2D images and down-sampled to the resolution of the other images for DCE-MRI analysis. The enhancing fraction (EF, fraction of tumor voxels with signal enhancement > 50% one minute after contrast agent administration) (19,20) and maps of IAUC₆₀ and the extended Tofts model parameters – K^{trans}, v_e, and v_p – were computed

from the DCE-MRI data. A previously measured population-based bi-exponential arterial input function (AIF) was used for pharmacokinetic analysis (21). Tumor-wise parameter medians were computed from the maps. Non-enhancing voxels and voxels with poor fits ($R^2 < 0.5$) were excluded from these computations and all subsequent analyses.

Micro-CT

Immediately after the final MRI session, mice were sacrificed by perfusion fixation and perfused with Microfil® (Flow Tech, Inc., Carver, MA, USA), a radiopaque vascular casting agent. Then, tumors were excised and scanned on a SkyScan 1176 micro-CT system (Bruker microCT, Kontich, BE) at 9- μm isotropic resolution. Tumor blood vessels were segmented from the micro-CT images using a Hessian-based filtering method (22,23). Tumor masks, which excluded any skin and subcutaneous fat remaining after excision, were manually drawn on the raw micro-CT images. From the segmented vessels and tumor masks, fractional blood volume (FBV), vessel surface area normalized to tumor volume (VSA), and median and 90th percentile distances to the nearest vessel (DNV and DNV90) were computed for each tumor. DNV is inversely related to overall vessel density, while DNV90 is sensitive to the presence of large avascular regions. These large avascular regions in the micro-CT images that corresponded to non-enhancing areas in the DCE-MRI image and necrotic areas in the histology sections were extracted from the tumor masks by thresholding the DNV maps. Thresholds were manually determined upon visual comparison of the three imaging modalities. These regions were excluded from the tumor volume measurements used to compute FBV and VSA. Details of the perfusion and micro-CT image acquisition, reconstruction, and processing can be found in (16).

Histology

After micro-CT imaging, the tumors were cut in half approximately along the MRI slice plane and embedded in paraffin. Four- μm -thick sections were cut from the center of each

tumor and stained with Hematoxylin Erythrosine Saffron (HES) for identifying viable tumor tissue, or double-stained with lectin (*Griffonia simplicifolia* lectin I, Vector Laboratories, Burlingame, CA, USA) as an endothelial marker for quantifying vascularization and anti-Ki67 antibody (monoclonal rabbit anti-human Ki67 with cross-reactivity to mouse; Abcam, Cambridge, UK) as a proliferation marker. Non-overlapping 10 \times fields were acquired from each lectin-stained tumor section using an Olympus BX41 microscope (Olympus Norge AS, Oslo, Norway). Six to 10 fields were acquired for each section to obtain good coverage of the viable tumor regions. RGB images were converted to HSV images, and lectin-stained endothelium was segmented by simple thresholding of the hue, saturation, and value channels. The same manually defined thresholds for each channel were used for all images. From the binarized images, the vascular area fraction was computed for each tumor.

Statistical analysis

All statistical analyses were performed in MATLAB (R2015a, MathWorks, Natick, MA, USA). Kruskal-Wallis one-way ANOVA was performed to test for a significant difference in normalized tumor volume between the three experimental groups on day 4. A two-tailed Wilcoxon rank-sum test was performed to test for a significant difference in normalized tumor volume between control and AVX235-treated tumors on day 7. One-way MANOVA, Kruskal-Wallis one-way ANOVA, and post-hoc Tukey's honest significant difference (HSD) tests were used for inter-group comparisons of micro-CT parameters and changes in DCE-MRI parameters. In addition to testing for differences in the multivariate means of multiple groups, the manova1 MATLAB function computes canonical variables – orthogonal linear combinations of the original predictor variables that maximize the separation between groups. Scatter plots of the first and second canonical variables were generated to visualize the separation between groups. Spearman correlation coefficients (ρ) were computed to measure the correlation between the “functional” DCE-MRI parameters (EF, IAUC₆₀, K^{trans}), micro-CT parameters, and histological vascular area fraction. For all tests, $\alpha = 0.05$.

Results

Pre-treatment DCE-MRI data was not acquired for one bevacizumab-treated mouse due to unsuccessful tail vein cannulation. From the micro-CT dataset, one control and one bevacizumab-treated tumor were excluded due to incomplete Microfil® perfusion.

Neither therapy resulted in early tumor growth inhibition

On day 0, the tumor volumes were 176 [135, 198.5] mm³ (median [25th quantile, 75th quantile]) for the control group, 192 [111.75, 199.25] mm³ for the AVX235-treated group, and 207 [196.5, 280] mm³ for the bevacizumab-treated group. Kruskal-Wallis one-way ANOVA and subsequent post-hoc Tukey's HSD tests showed that the median day 0 tumor volume was significantly larger in the bevacizumab group than in the AVX235 group ($P = 0.042$). Therefore, tumor volumes were normalized to day 0 values to evaluate the therapeutic effects on tumor growth (**Figure 1**). There were no significant differences in median normalized tumor volumes between the three groups on day 4 ($P = 0.135$, one-way ANOVA), or between the control and AVX235 groups on day 7 ($P = 0.200$, two-tailed Wilcoxon rank-sum test).

DCE-MRI did not detect differential treatment responses

One-way MANOVA determined that there were no significant differences between the three groups based on the pre- to post-treatment changes in the DCE-MRI parameters ($P = 0.330$). This is visualized by the scatter plot of the first and second canonical variables (c1 vs. c2), which shows a high degree of overlap between the groups (**Figure 2 a**). There is some partial separation between the control and bevacizumab-treated groups, with the AVX235-treated group in between. When looking at the DCE-MRI parameters individually (**Figure 2 b-f**), it becomes apparent that bevacizumab had therapeutic effects, e.g., there was a clear decrease in IAUC₆₀ (**Figure 2 c**). However,

when accounting for multiple groups and parameters, these effects were not statistically significant.

Micro-CT revealed treatment-related differences in vascular morphology

Micro-CT revealed significant differences in vascular morphology between the experimental groups ($P < 0.001$, one-way MANOVA). There is a clear separation between the bevacizumab-treated group and the other two groups along c1, and good separation between the AVX235-treated and control groups along c2 (**Figure 3 a**).

VSA, and FBV were largest in the control group and smallest in the bevacizumab group (**Figure 3 b-c**), and the opposite trend was observed for DNV (**Figure 3 d**). These parameters were significantly different in the bevacizumab group compared to controls ($P < 0.01$, post-hoc Tukey's HSD test). There was a significant difference in VSA between the AVX235 and bevacizumab groups ($P < 0.05$). The difference in FBV between the two treatment groups was close to statistical significance ($P = 0.054$). AVX235-treated tumors had the largest DNV90 (**Figure 3 e**), which was significantly different from the DNV90 in control tumors ($P < 0.01$).

DCE-MRI functional parameters correlate with micro-CT vascular morphometrics

Pooled (all tumors from all groups) and group-wise Spearman ρ values between DCE-MRI and micro-CT parameters are presented in **Table 1**.

With the groups pooled, there was a moderate but significant positive correlation between IAUC₆₀ and VSA ($P = 0.019$); K^{trans} also positively correlated with VSA ($P = 0.008$). There was a negative correlation between EF and DNV90 ($P = 0.048$).

The correlation coefficients for individual groups revealed interesting effects of treatment on the relationship between DCE-MRI and micro-CT measurements. First, there were no significant correlations in the control group. Second, the correlations in the bevacizumab group were of the opposite sign as those in the AVX235 group.

Figures 4 and **5** present these trends. With all three groups pooled, IAUC₆₀ and K^{trans} generally increased with VSA and FBV (**Figure 4**). This was also the case for the AVX235 group on its own. The DCE-MRI and micro-CT parameter values were lower in the bevacizumab group than in the other groups, contributing to the pooled positive correlations. However, there was a negative correlation between the DCE-MRI and micro-CT parameters within the bevacizumab group.

Despite this unexpected inverse relationship in the bevacizumab group, we qualitatively observed a direct spatial relationship between DCE-MRI and micro-CT within individual tumors. **Figure 5 c** illustrates this – the top tumor is less vascularized than the bottom based on the micro-CT data (center column), but has greater IAUC₆₀ in the viable tumor area (left); but within each tumor, relatively highly vascularized areas correspond to high perfusion (central region of the top tumor) and vice versa (lower right region of the bottom tumor).

Tumor perfusion inversely correlates with histological vascularization

Overall, there was a moderate but significant ($P = 0.018$) negative correlation between IAUC₆₀ and histological vascular area fraction (**Table 2**, **Figure 6 a**). The intra-group correlation between IAUC₆₀ and vascular area fraction was significant for the control group; the intra-group correlation between K^{trans} and vascular area fraction was significant for the control and bevacizumab groups (**Table 2**, **Figure 6 a-b**).

There were no significant correlations between histological vascular area fraction and the micro-CT parameters (**Table 2**, **Figure 6 c-d**). The correlation with FBV in the bevacizumab group was good but fell just short of statistical significance ($P = 0.058$). Of note, the correlations between micro-CT and histologically measured vascularization were positive in the bevacizumab group while all other correlations were negative or very weak.

Discussion

While tumor growth inhibition did not reach statistical significance within the time frame of this experiment, previous studies have demonstrated that both AVX235 and bevacizumab inhibit vascular proliferation and long-term tumor growth in the MAS98.12 model used here (16,18). The DCE-MRI data from this study indicate that the two drugs did not have significantly different effects, but the micro-CT data did reveal significant differences between the experimental groups. The differences between groups are further emphasized by the correlations between the DCE-MRI and micro-CT parameters. Before comparing the group-wise correlations, it is worth discussing the pooled correlations and the general dependence of DCE-MRI functional parameters on vascular structure.

Pooled correlations show that vascular structure influences DCE-MRI parameters

The significant positive correlations between IAUC₆₀ and K^{trans} and VSA demonstrate that DCE-MRI parameters are not only influenced by vascular function, but can also be highly dependent on vascular surface area (4). The commonly used extended Tofts model is most appropriate and accurate under high flow conditions in which contrast agent extravasation is PS-limited (24). Pharmacokinetic analysis can be restricted to fast-enhancing voxels to ensure that the data satisfies this condition, as was done here. In addition, most tumor blood vessels are characteristically leaky and thus highly permeable to the low molecular weight gadolinium-based contrast agents used in the clinic. Thus, vascular surface area can be the determining factor in contrast agent kinetics in some cases.

It may seem contradictory that IAUC₆₀ correlated positively with VSA but negatively with histological vascular area fraction. However, the three imaging modalities report different things about the vasculature. This makes it difficult to use one technique to validate another, but combining these complementary image data can provide deeper, more nuanced insights into tumor vascular biology. To make sound interpretations, one must be mindful of exactly what these methods measure and how they differ. DCE-MRI characterizes tumor perfusion via functional vessels, micro-CT visualizes the structure of

these functional vessels, and histological staining marks endothelial cells regardless of vessel functionality.

The lack of correlation between micro-CT and histology can be explained by the dysfunctional nature of tumor vasculature, combined with the different vessel populations that are detected by each imaging modality. The negative correlation between DCE-MRI and histology suggests that increased vascularization from dysregulated tumor angiogenesis does not always translate to increased perfusion and may actually be counterproductive. **Figure 5 b** (top row) and **Figure 5 c** (bottom row) show examples of tumor regions that were not perfused based on DCE-MRI and micro-CT but were still viable and vascularized based on histology.

Similarly, a previous study found a negative correlation between K^{trans} and histological microvessel density in colorectal cancer xenografts (25). But other studies have reported moderate to strong positive correlations between DCE-MRI and histological parameters (9,10,26), while others showed weak or no correlations (27-29). These discrepancies could be due to the wide range of data acquisition and analysis methods that were employed; or to the different patient populations, preclinical cancer models, or treatment regimens investigated. Considering the high degree of heterogeneity between different types of cancer and even within the same cancer type, there is likely concomitant heterogeneity in the relationship between tumor vascularization and perfusion.

Group-wise correlations illustrate the complexity and mutability of the interpretation of DCE-MRI parameters

The group-wise correlations revealed interesting and unexpected differences between the three experimental groups. The lack of significant correlations between DCE-MRI and micro-CT parameters in the control group suggests large inter-tumor heterogeneity in vascular phenotype or a decoupling of structure and function in the tumor vasculature. This may be a consequence of the characteristically chaotic and hyperpermeable vessels that are produced by pathological tumor angiogenesis. In contrast, the direct relationships

between DCE-MRI and micro-CT in the AVX235-treated tumors suggest that cPLA2 inhibition resulted in vascular normalization and subsequent recoupling of vascular structure and function.

Analogously, a recent study showed that K^{trans} did not correlate with an independent measure of PS product (made by quantifying the leakage of a radioactive tracer) in the control group of a rat model of lung cancer brain metastasis. But there was a positive correlation after bevacizumab treatment, which the authors attributed to therapy-induced vascular normalization (30).

The inverse associations in the bevacizumab-treated group in our study are harder to interpret but may indicate improved blood flow as a result of treatment-induced vascular pruning and remodeling. This hypothesis is supported by the increase in EF and borderline significant positive correlation between FBV and histological vascular area fraction in the bevacizumab group, i.e., after bevacizumab treatment, the amount of functional vasculature is more closely associated with the total amount of vasculature, as is expected in healthy tissue. The negative correlations between DCE-MRI and micro-CT, then, reflect the negative correlation between DCE-MRI and histology.

This suggests that in the bevacizumab group, contrast-agent delivery to the tumor was not directly determined by vascular surface area but instead by blood flow. Given that dysregulated angiogenesis and subsequent hypervascularization can lead to vascular insufficiency in tumors, it is reasonable that fewer, well-functioning vessels can deliver greater blood flow (31,32). One possible mechanistic explanation for this is that decreased vascular permeability resulted in decreased tumor interstitial fluid pressure (a previously reported effect of bevacizumab treatment) and thus improved tumor perfusion and delivery of contrast agent to the tumor tissue (33-35).

This could also explain the increase in EF seen after bevacizumab treatment. While EF often decreases after anti-angiogenic and anti-vascular therapies (7,19,36), other studies have reported treatment-induced increases in EF, including a previous study investigating the effects of bevacizumab on the tumor model used here (20,37,38).

The disparate correlations between the treatment groups could be the consequence of two distinct mechanisms of action leading to differential modifications of the tumor vasculature. Alternatively, the difference could represent two distinct time points in a common pharmacological progression. Despite the large amount of research on tumor angiogenesis and anti-angiogenic therapy, the mechanisms of action of these drugs are still not fully understood (39). The results presented here reflect this complexity of tumor biology and pharmacodynamics.

Study limitations

Limitations of this study include the use of a single population-based AIF, which could have changed significantly during treatment, and manual injection of contrast agents. The use of a power injector for DCE-MRI would have resulted in more uniform AIFs across animals and time points, and a perfusion pump would have ensured consistent Microfil® perfusion at physiological pressures and thus minimized vessel distortion. Another limitation was the nine-micron spatial resolution of the micro-CT scanner, which is not enough to detect the smallest capillary-sized vessels. This may have biased the data if the proportion of these microvessels varied between experimental groups. As mentioned above, postmortem staining of blood vessels in histological sections does not discriminate between perfused and non-perfused vessels. For the purposes of validating DCE-MRI and other *in vivo* perfusion imaging techniques, methods such as labeling functional vessels via intravital lectin perfusion would be more suitable (40). Given some of the unexpected correlations found in this study, the generalizability and reproducibility of these vascular structure-function associations should be tested using different tumor models, therapies, and contrast agents.

Conclusions

DCE-MRI parameters such as IAUC₆₀ and K^{trans}, largely regarded as measures of vessel permeability or blood flow (i.e., vascular function), can be greatly influenced by vascular

surface area. The relative weights of these three factors can be significantly altered by anti-angiogenic therapy, making the interpretation of DCE-MRI measurements difficult. This highlights one of the challenges of adopting DCE-MRI parameters as clinical biomarkers and emphasizes the need for a better understanding of tumor angiogenesis and of the mechanisms of action of anti-angiogenic agents.

Acknowledgements

This work was funded by the liaison committee between the Central Norway Regional Health Authority and the Norwegian University of Science and Technology (NTNU) (grant no. 46056806), the Norwegian Cancer Society (grant no. 2209215), the Research Council of Norway (grants no. 239940 and 228879; BIA grant no. 193203), and Avexxin AS. The MR imaging was performed at the NTNU MR Core Facility. Animals were housed and treated by the NTNU Comparative Medicine Core Facility. The core facilities are funded by the Faculty of Medicine at NTNU and the Central Norway Regional Health Authority. We thank Alexandre Kristian at the Department of Oncology and Department of Tumor Biology, Oslo University Hospital, for performing the xenograft transplants.

References

1. O'Connor JP, Jackson A, Parker GJ, Roberts C, Jayson GC. Dynamic contrast-enhanced MRI in clinical trials of antivascular therapies. *Nat Rev Clin Oncol* 2012;9(3):167-177.
2. Leach MO, Brindle KM, Evelhoch JL, Griffiths JR, Horsman MR, Jackson A, Jayson GC, Judson IR, Knopp MV, Maxwell RJ, McIntyre D, Padhani AR, Price P, Rathbone R, Rustin GJ, Tofts PS, Tozer GM, Vennart W, Waterton JC, Williams SR, Workman P, Pharmacodynamic/Pharmacokinetic Technologies Advisory Committee DDOCRUK. The assessment of antiangiogenic and antivascular therapies in early-stage clinical trials using magnetic resonance imaging: issues and recommendations. *Br J Cancer* 2005;92(9):1599-1610.

3. Evelhoch JL. Key factors in the acquisition of contrast kinetic data for oncology. *J Magn Reson Imaging* 1999;10(3):254-259.
4. Tofts PS, Brix G, Buckley DL, Evelhoch JL, Henderson E, Knopp MV, Larsson HB, Lee TY, Mayr NA, Parker GJ, Port RE, Taylor J, Weisskoff RM. Estimating kinetic parameters from dynamic contrast-enhanced T(1)-weighted MRI of a diffusible tracer: standardized quantities and symbols. *J Magn Reson Imaging* 1999;10(3):223-232.
5. Sung YS, Park B, Choi Y, Lim HS, Woo DC, Kim KW, Kim JK. Dynamic contrast-enhanced MRI for oncology drug development. *J Magn Reson Imaging* 2016;44(2):251-264.
6. Batchelor TT, Sorenson AG, di Tomaso E, Zhang WT, Duda DG, Cohen KS, Kozak KR, Cahill DP, Chen PJ, Zhu M, Ancukiewicz M, Mrugala MM, Plotkin S, Drappatz J, Louis DN, Ivy P, Scadden DT, Benner T, Loeffler JS, Wen PY, Jain RK. AZD2171, a pan-VEGF receptor tyrosine kinase inhibitor, normalizes tumor vasculature and alleviates edema in glioblastoma patients. *Cancer Cell* 2007;11(1):83-95.
7. O'Connor JP, Carano RA, Clamp AR, Ross J, Ho CC, Jackson A, Parker GJ, Rose CJ, Peale FV, Friesenhahn M, Mitchell CL, Watson Y, Roberts C, Hope L, Cheung S, Reslan HB, Go MA, Pacheco GJ, Wu X, Cao TC, Ross S, Buonaccorsi GA, Davies K, Hasan J, Thornton P, del Puerto O, Ferrara N, van Bruggen N, Jayson GC. Quantifying antivascular effects of monoclonal antibodies to vascular endothelial growth factor: insights from imaging. *Clin Cancer Res* 2009;15(21):6674-6682.
8. Sourbron SP, Buckley DL. Tracer kinetic modelling in MRI: estimating perfusion and capillary permeability. *Phys Med Biol* 2012;57(2):R1-33.
9. Buckley DL, Drew PJ, Mussurakis S, Monson JR, Horsman A. Microvessel density of invasive breast cancer assessed by dynamic Gd-DTPA enhanced MRI. *J Magn Reson Imaging* 1997;7(3):461-464.
10. Sterzik A, Paprottka PM, Zengel P, Hirner H, Rosspunt S, Eschbach R, Moser M, Havla L, Ingrisch M, Mack B, Reiser MF, Nikolaou K, Cyran CC. DCE-MRI biomarkers for monitoring an anti-angiogenic triple combination therapy in experimental hypopharynx carcinoma xenografts with immunohistochemical validation. *Acta Radiol* 2015;56(3):294-303.

11. Gaustad JV, Brurberg KG, Simonsen TG, Mollatt CS, Rofstad EK. Tumor vascularity assessed by magnetic resonance imaging and intravital microscopy imaging. *Neoplasia* 2008;10(4):354-362.
12. Kerbel RS. Tumor angiogenesis. *N Engl J Med* 2008;358(19):2039-2049.
13. Kokotos G, Feuerherm AJ, Barbayianni E, Shah I, Sæther M, Magriot V, Nguyen T, Constantinou-Kokotou V, Dennis EA, Johansen B. Inhibition of Group IVA Cytosolic Phospholipase A2 by Thiazolyl Ketones in Vitro, ex Vivo, and in Vivo. *Journal of medicinal chemistry* 2014(Figure 1).
14. Linkous AG, Yazlovitskaya EM, Hallahan DE. Cytosolic phospholipase A2 and lysophospholipids in tumor angiogenesis. *J Natl Cancer Inst* 2010;102(18):1398-1412.
15. Patel MI, Singh J, Niknami M, Kurek C, Yao M, Lu S, Maclean F, King NJ, Gelb MH, Scott KF, Russell PJ, Boulas J, Dong Q. Cytosolic phospholipase A2-alpha: a potential therapeutic target for prostate cancer. *Clin Cancer Res* 2008;14(24):8070-8079.
16. Kim E, Tunset HM, Cebulla J, Vettukattil R, Helgesen H, Feuerherm AJ, Engebraten O, Maelandsmo GM, Johansen B, Moestue SA. Anti-vascular effects of the cytosolic phospholipase A2 inhibitor AVX235 in a patient-derived basal-like breast cancer model. *BMC Cancer* 2016;16(1):191.
17. Bergamaschi A, Hjortland GO, Triulzi T, Sørlie T, Johnsen H, Ree AH, Russnes HG, Tronnes S, Maelandsmo GM, Fodstad O, Borresen-Dale A-L, Engebraaten O. Molecular profiling and characterization of luminal-like and basal-like in vivo breast cancer xenograft models. *Molecular oncology* 2009;3(5-6):469-482.
18. Lindholm EM, Kristian A, Nalwoga H, Kruger K, Nygard S, Akslen LA, Maelandsmo GM, Engebraaten O. Effect of antiangiogenic therapy on tumor growth, vasculature and kinase activity in basal- and luminal-like breast cancer xenografts. *Mol Oncol* 2012;6(4):418-427.
19. Galbraith SM, Maxwell RJ, Lodge MA, Tozer GM, Wilson J, Taylor NJ, Stirling JJ, Sena L, Padhani AR, Rustin GJ. Combretastatin A4 phosphate has tumor antivascular activity in rat and man as demonstrated by dynamic magnetic resonance imaging. *J Clin Oncol* 2003;21(15):2831-2842.

20. Cebulla J, Huuse EM, Pettersen K, van der Veen A, Kim E, Andersen S, Prestvik WS, Bofin AM, Pathak AP, Bjorkoy G, Bather TF, Moestue SA. MRI reveals the in vivo cellular and vascular response to BEZ235 in ovarian cancer xenografts with different PI3-kinase pathway activity. *Br J Cancer* 2015;112(3):504-513.
21. Jensen LR, Huuse EM, Bather TF, Goa PE, Bofin AM, Pedersen TB, Lundgren S, Gribbestad IS. Assessment of early docetaxel response in an experimental model of human breast cancer using DCE-MRI, ex vivo HR MAS, and in vivo 1H MRS. *NMR Biomed* 2010;23(1):56-65.
22. Kim E, Cebulla J, Ward BD, Rhie K, Zhang J, Pathak AP. Assessing breast cancer angiogenesis in vivo: Which susceptibility contrast MRI biomarkers are relevant? *Magnetic Resonance in Medicine* 2013;70(4):1106-1116.
23. Sato Y, Nakajima S, Shiraga N, Atsumi H, Yoshida S, Koller T, Gerig G, Kikinis R. Three-dimensional multi-scale line filter for segmentation and visualization of curvilinear structures in medical images. *Med Image Anal* 1998;2(2):143-168.
24. Sourbron SP, Buckley DL. On the scope and interpretation of the Tofts models for DCE-MRI. *Magn Reson Med* 2011;66(3):735-745.
25. Ahn SJ, An CS, Koom WS, Song HT, Suh JS. Correlations of 3T DCE-MRI quantitative parameters with microvessel density in a human-colorectal-cancer xenograft mouse model. *Korean J Radiol* 2011;12(6):722-730.
26. Schlemmer HP, Merkle J, Grobholz R, Jaeger T, Michel MS, Werner A, Rabe J, van Kaick G. Can pre-operative contrast-enhanced dynamic MR imaging for prostate cancer predict microvessel density in prostatectomy specimens? *Eur Radiol* 2004;14(2):309-317.
27. Franiel T, Ludemann L, Rudolph B, Rehbein H, Stephan C, Taupitz M, Beyersdorff D. Prostate MR imaging: tissue characterization with pharmacokinetic volume and blood flow parameters and correlation with histologic parameters. *Radiology* 2009;252(1):101-108.
28. Su MY, Cheung YC, Fruehauf JP, Yu H, Nalcioglu O, Mechetner E, Kyshtoobayeva A, Chen SC, Hsueh S, McLaren CE, Wan YL. Correlation of dynamic contrast enhancement MRI parameters with microvessel density and VEGF for assessment of angiogenesis in breast cancer. *J Magn Reson Imaging* 2003;18(4):467-477.

29. van Niekerk CG, van der Laak JA, Hambrock T, Huisman HJ, Witjes JA, Barentsz JO, Hulsbergen-van de Kaa CA. Correlation between dynamic contrast-enhanced MRI and quantitative histopathologic microvascular parameters in organ-confined prostate cancer. *Eur Radiol* 2014;24(10):2597-2605.
30. Pishko GL, Muldoon LL, Pagel MA, Schwartz DL, Neuwelt EA. Vascular endothelial growth factor blockade alters magnetic resonance imaging biomarkers of vascular function and decreases barrier permeability in a rat model of lung cancer brain metastasis. *Fluids Barriers CNS* 2015;12:5.
31. Jain RK. Normalization of tumor vasculature: an emerging concept in antiangiogenic therapy. *Science* 2005;307(5706):58-62.
32. Ziyad S, Iruela-Arispe ML. Molecular mechanisms of tumor angiogenesis. *Genes Cancer* 2011;2(12):1085-1096.
33. Willett CG, Boucher Y, di Tomaso E, Duda DG, Munn LL, Tong RT, Chung DC, Sahani DV, Kalva SP, Kozin SV, Mino M, Cohen KS, Scadden DT, Hartford AC, Fischman AJ, Clark JW, Ryan DP, Zhu AX, Blaszkowsky LS, Chen HX, Shellito PC, Lauwers GY, Jain RK. Direct evidence that the VEGF-specific antibody bevacizumab has antivascular effects in human rectal cancer. *Nat Med* 2004;10(2):145-147.
34. Salnikov AV, Heldin NE, Stuhr LB, Wiig H, Gerber H, Reed RK, Rubin K. Inhibition of carcinoma cell-derived VEGF reduces inflammatory characteristics in xenograft carcinoma. *Int J Cancer* 2006;119(12):2795-2802.
35. Gremonprez F, Descamps B, Izmer A, Vanhove C, Vanhaecke F, De Wever O, Ceelen W. Pretreatment with VEGF(R)-inhibitors reduces interstitial fluid pressure, increases intraperitoneal chemotherapy drug penetration, and impedes tumor growth in a mouse colorectal carcinomatosis model. *Oncotarget* 2015;6(30):29889-29900.
36. Messiou C, Orton M, Ang JE, Collins DJ, Morgan VA, Mears D, Castellano I, Papadatos-Pastos D, Brunetto A, Tunariu N, Mann H, Tessier J, Young H, Ghiorghiu D, Marley S, Kaye SB, deBono JS, Leach MO, deSouza NM. Advanced solid tumors treated with cediranib: comparison of dynamic contrast-enhanced MR imaging and CT as markers of vascular activity. *Radiology* 2012;265(2):426-436.
37. Jayson GC, Parker GJ, Mullamitha S, Valle JW, Saunders M, Broughton L, Lawrance J, Carrington B, Roberts C, Issa B, Buckley DL, Cheung S, Davies K, Watson Y, Zinkewich-

- Peotti K, Rolfe L, Jackson A. Blockade of platelet-derived growth factor receptor-beta by CDP860, a humanized, PEGylated di-Fab', leads to fluid accumulation and is associated with increased tumor vascularized volume. *J Clin Oncol* 2005;23(5):973-981.
38. Moestue SA, Huuse EM, Lindholm EM, Bofin A, Engebraaten O, Maelandsmo GM, Akslen LA, Gribbestad IS. Low-molecular contrast agent dynamic contrast-enhanced (DCE)-MRI and diffusion-weighted (DW)-MRI in early assessment of bevacizumab treatment in breast cancer xenografts. *J Magn Reson Imaging* 2013;38(5):1043-1053.
39. Welti J, Loges S, Dimmeler S, Carmeliet P. Recent molecular discoveries in angiogenesis and antiangiogenic therapies in cancer. *J Clin Invest* 2013;123(8):3190-3200.
40. Debbage PL, Griebel J, Ried M, Gneiting T, DeVries A, Hutzler P. Lectin intravital perfusion studies in tumor-bearing mice: micrometer-resolution, wide-area mapping of microvascular labeling, distinguishing efficiently and inefficiently perfused microregions in the tumor. *J Histochem Cytochem* 1998;46(5):627-639.

Figures

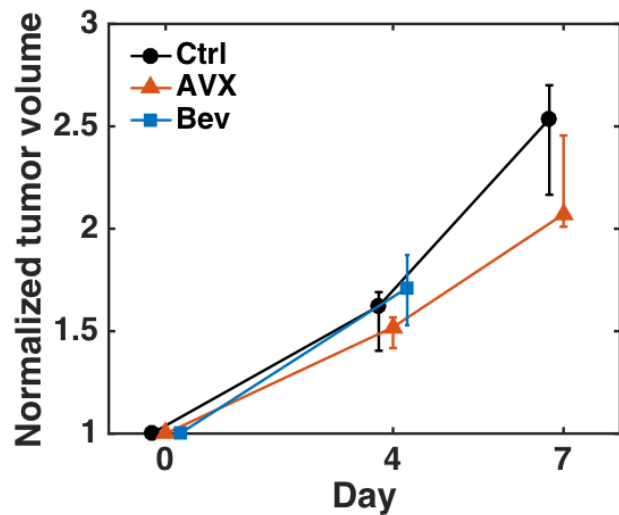


Figure 1: Tumor growth curves. The tumor volumes were determined from 3D MR images and normalized to pre-treatment (day 0) values. The data points and error bars represent the medians and interquartile ranges. Ctrl: control, AVX: AVX235-treated, Bev: bevacizumab-treated.

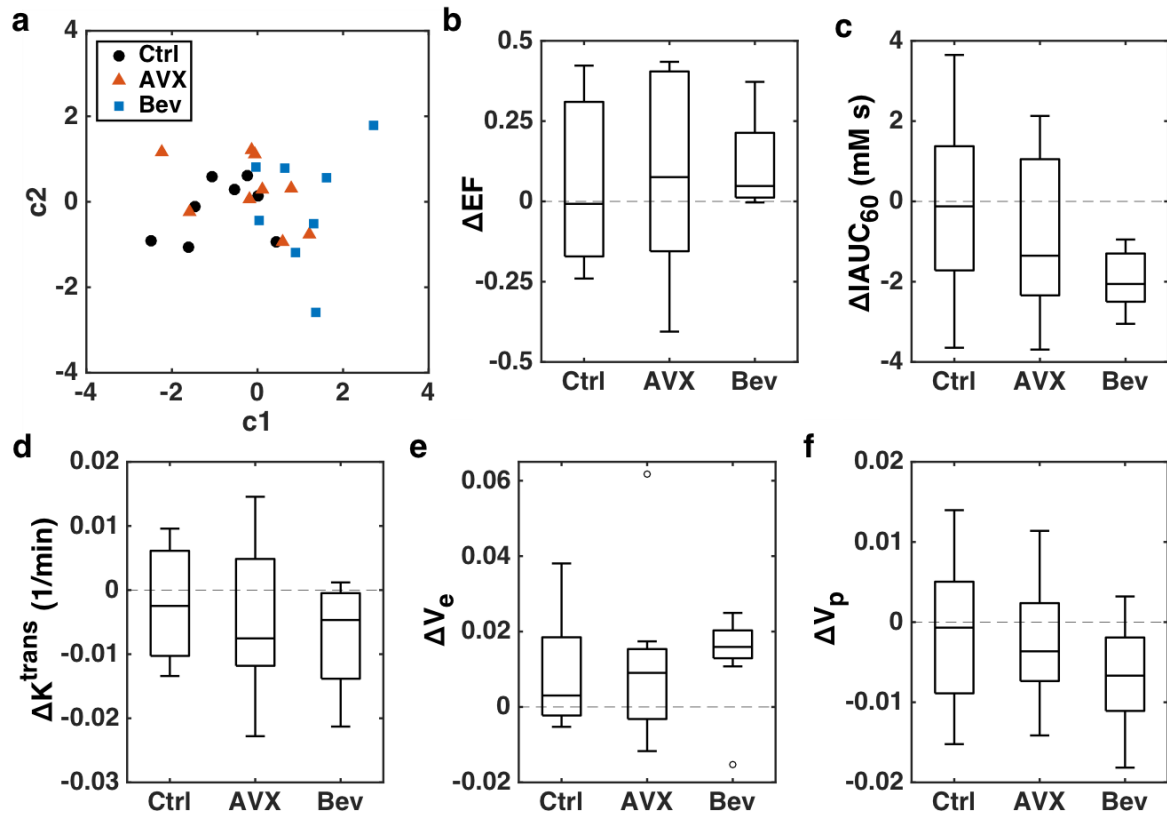


Figure 2: a) Tumor-wise scatter plot of the first vs. second canonical variables (c_1 vs. c_2) determined by one-way MANOVA of all DCE-MRI parameters (EF, IAUC₆₀, K^{trans} , v_e , and v_p). b-f) Box plots of the changes in DCE-MRI parameters from pre- to post-treatment. Ctrl: control, AVX: AVX235-treated, Bev: bevacizumab-treated.

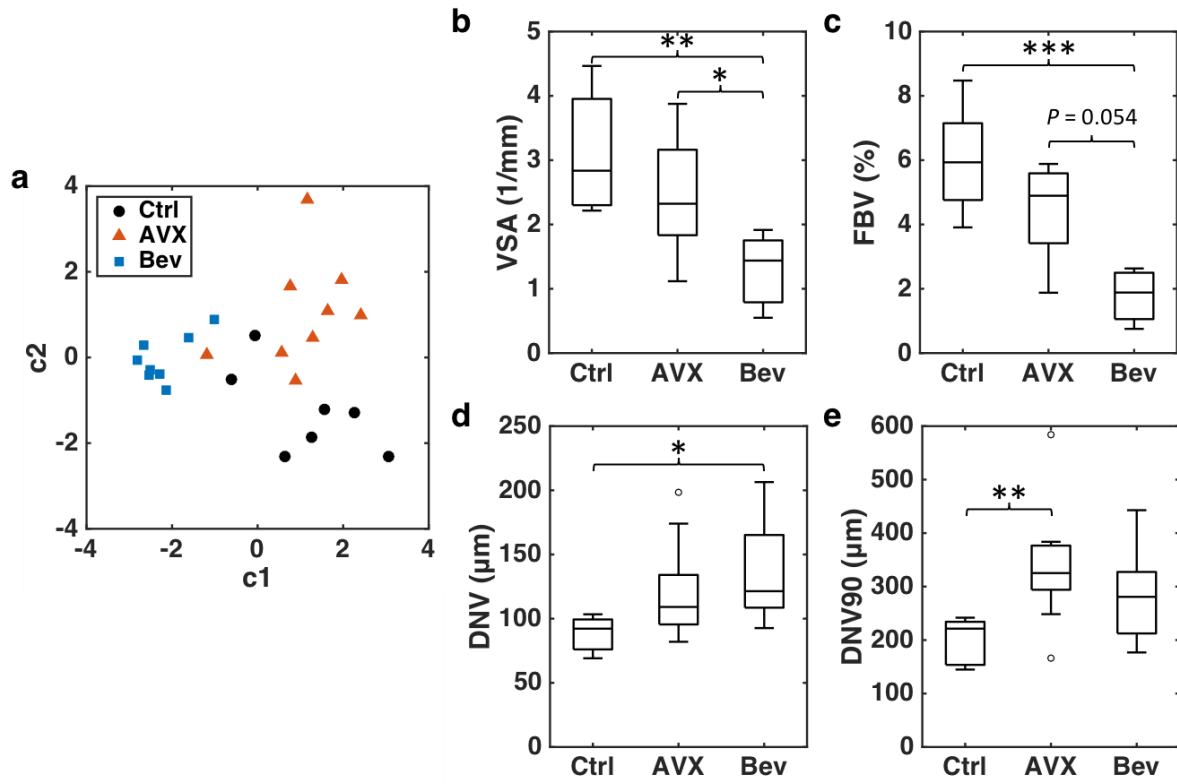


Figure 3: a) Tumor-wise scatter plot of the first vs. second canonical variables (c1 vs. c2) determined by one-way MANOVA of all micro-CT parameters (VSA, FBV, DNV and DNV90). b-e) Box plots of the micro-CT parameters. Ctrl: control, AVX: AVX235-treated, Bev: bevacizumab-treated. P -values are from post-hoc Tukey's HSD tests performed after Kruskal-Wallis one-way ANOVA. * $P < 0.05$, ** $P < 0.01$, *** $P < 0.001$.

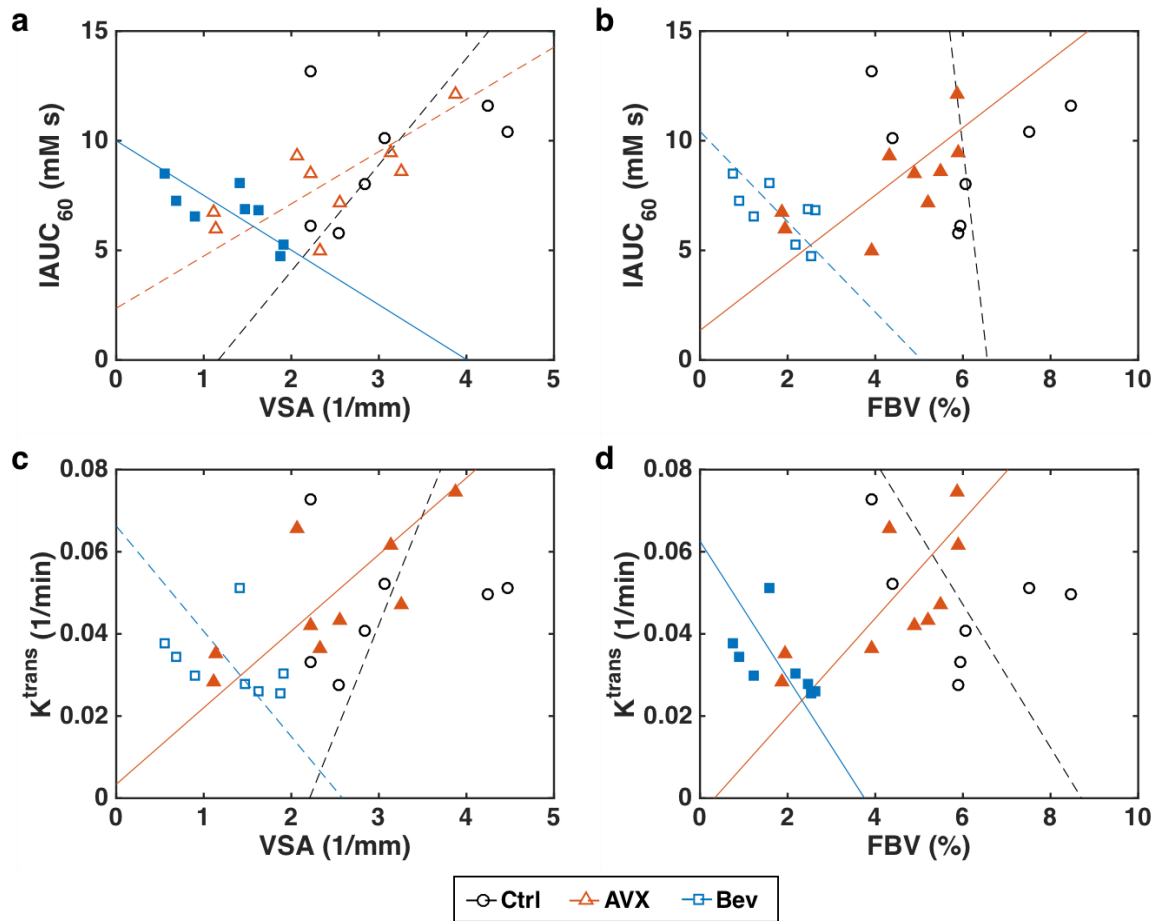


Figure 4: Tumor-wise scatter plots of select DCE-MRI vs. micro-CT parameters, and the corresponding Deming regression lines for each group. Filled-in data points and solid regression lines indicate statistically significant intra-group Spearman correlations ($P < 0.05$). Ctrl: control, AVX: AVX235-treated, Bev: bevacizumab-treated.

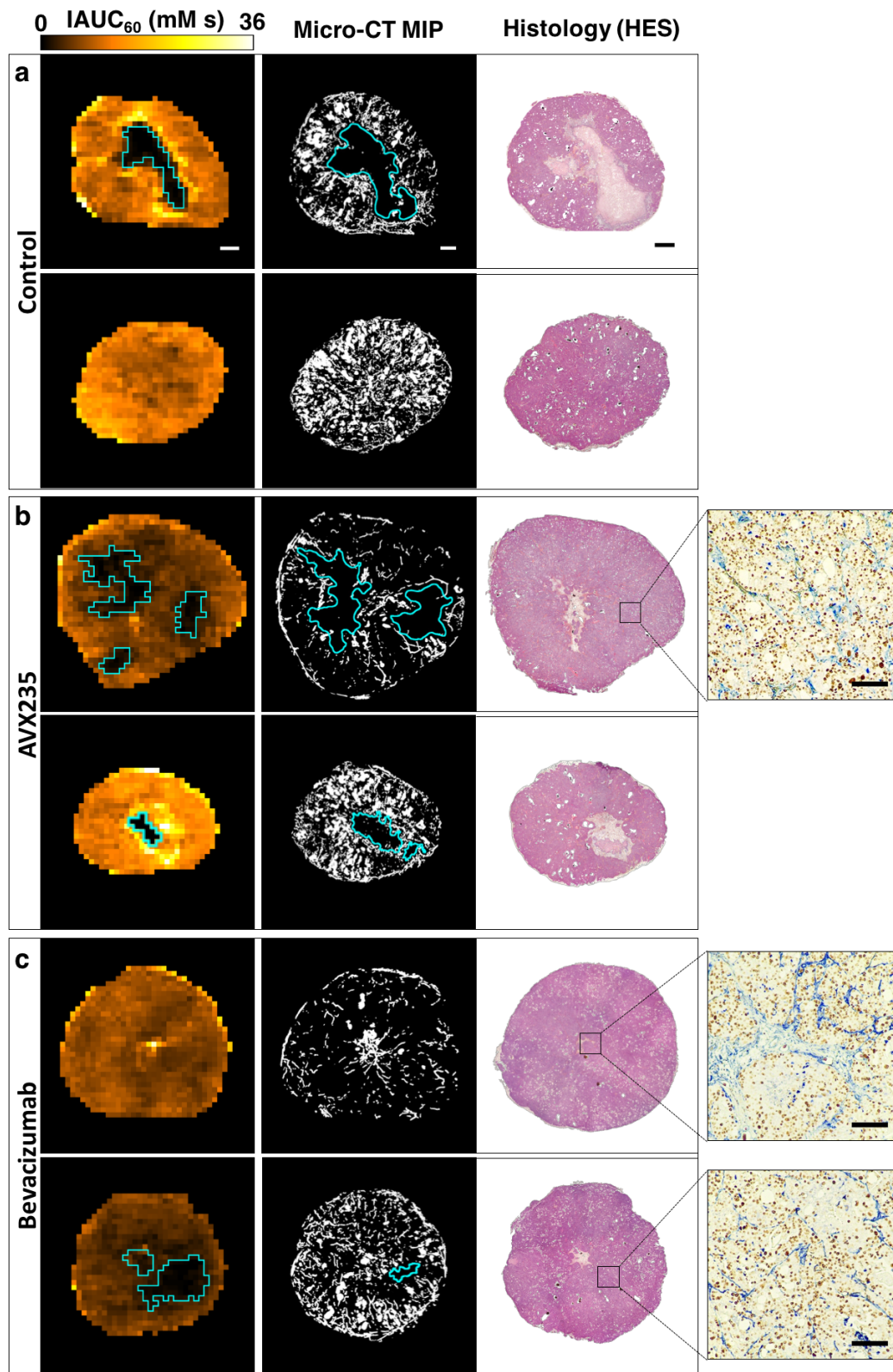


Figure 5: Two example tumors from the a) control, b) AVX235, and c) bevacizumab groups. For each group, the top tumor has a smaller FBV than the bottom tumor. Left column: a slice of the IAUC₆₀ map (0.6 mm slice thickness). Center column: 540-μm-thick (60 slices) maximum intensity projection (MIP) of the segmented micro-CT vasculature from the same region. Non-enhancing or non-perfused tumor regions in the DCE-MRI and micro-CT images that were excluded from the data analysis are outlined in cyan. Right column: corresponding HES-stained histology section. Insets: fields from adjacent sections double-stained with lectin (blue) and anti-Ki67 antibody (brown), scale bars = 200 μm. Top row scale bars = 1 mm.

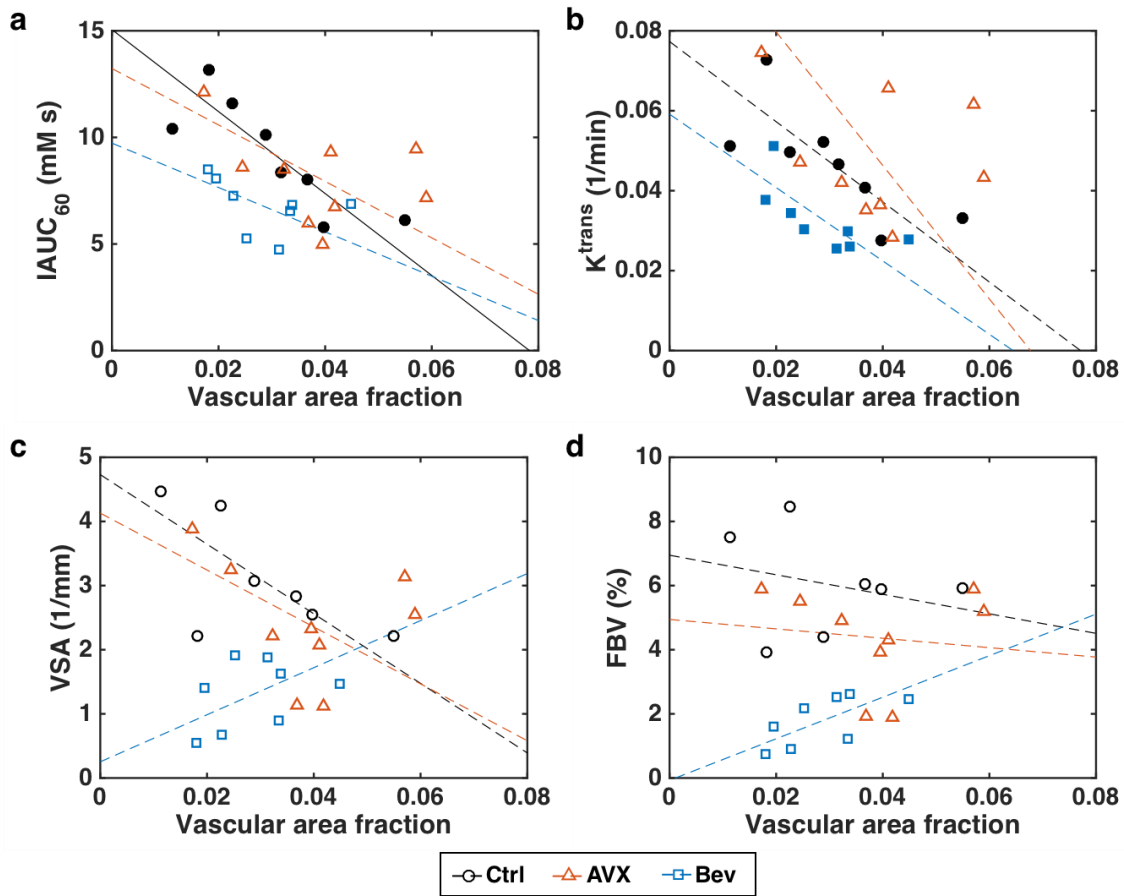


Figure 6: Tumor-wise scatter plots of select DCE-MRI and micro-CT parameters vs. histological vascular area fraction, and the corresponding Deming regression lines for each group. Filled-in data points and solid regression lines indicate statistically significant intra-group Spearman correlations ($P < 0.05$). Ctrl: control, AVX: AVX235-treated, Bev: bevacizumab-treated.

Tables

Table 1. Spearman correlation coefficients (ρ) between DCE-MRI and micro-CT parameters

		VSA	FBV	DNV	DNV90
EF	Pooled^a	-0.125	-0.202	-0.094	-0.407
	Ctrl^b	0.714	0.607	-0.393	-0.464
	AVX^c	0.383	0.183	-0.55	-0.767
	Bev^d	-0.738	-0.786	0.619	0.548
IAUC ₆₀	Pooled^a	0.475	0.354	-0.337	-0.236
	Ctrl^b	0.179	0.036	0.000	-0.321
	AVX^c	0.617	0.800	-0.733	-0.700
	Bev^d	-0.786	-0.619	0.690	0.714
K^{trans}	Pooled^a	0.527	0.356	-0.319	-0.129
	Ctrl^b	0.107	-0.321	0.214	-0.107
	AVX^c	0.717	0.800	-0.767	-0.833
	Bev^d	-0.595	-0.786	0.429	0.381

Ctrl: control, AVX: AVX235-treated, Bev: bevacizumab-treated

^an = 24, ^bn = 7, ^cn = 9, ^dn = 8

Bold: ρ is significantly different than zero, $P < 0.05$, *t*-test

Table 2. Spearman correlation coefficients (ρ) between histological vascular area fraction and DCE-MRI and micro-CT parameters

	Pooled	Ctrl	AVX ^e	Bev ^c
IAUC₆₀	-0.484^a	-0.857^c	-0.217	-0.548
K^{trans}	-0.350 ^a	-0.786^c	-0.217	-0.810
VSA	-0.078 ^b	-0.464 ^d	-0.333	0.476
FBV	0.104 ^b	-0.143 ^d	-0.133	0.714

Ctrl: control, AVX: AVX235-treated, Bev: bevacizumab-treated

^an = 25, ^bn = 24, ^cn = 8, ^dn = 7, ^en = 9

Bold: ρ is significantly different than zero, $P < 0.05$, *t*-test